J. Electr. Electron. Mater.
Vol. 39, No. 2, pp. 129-146 March 2026
doi: https://doi.org/10.4313/JEEM.2026.39.2.3
ISSN 1226-7945(Print), 2288-3258(Online)

Academic Progress Report

Recent Progress on Transition Metal-Based Oxygen Evolution Reaction Electrocatalysts in Alkaline Medium

Gyeongbae Park[1], Da-Un Han[1,2], Won Rae Kim[1], and Seung-Min Yang[1]

[1]Functional Materials and Components Group, Korea Institute of Industrial Technology, Gangneung 25440, Korea

[2]Department of Materials Science and Engineering, Hanyang University, Seoul 04763, Korea

(Received January 3, 2026; Revised January 20, 2026; Accepted January 22, 2026)

Abstract: Electrochemical water splitting has emerged as a pivotal technology for green hydrogen production, offering a viable pathway toward a sustainable energy future. Among various electrolysis systems, Anion exchange membrane water electrolysis is particularly noteworthy as a cost-effective solution capable of operating under the fluctuating power inputs typical of renewable energy sources. However, the overall efficiency of water splitting is fundamentally limited by the oxygen evolution reaction, which exhibits sluggish kinetics compared to the hydrogen evolution reaction. While IrO_2 and RuO_2 serve as current benchmarks, their scarcity and high cost necessitate the development of earth-abundant alternatives. This review provides a comprehensive overview of fundamental OER mechanisms including the adsorbate evolution mechanism, lattice oxygen mechanism, and oxide path mechanism while highlighting how new pathways can circumvent traditional scaling relations. We discuss recent advancements in transition metal-based electrocatalysts, encompassing oxides, hydroxides, chalcogenides, phosphides, nitrides, and carbides, with a focus on innovative design strategies such as defect engineering, heteroatom doping, and heterostructure construction. This paper concludes by addressing current challenges and offering perspectives on future directions for the development of highly efficient and economically viable oxygen evolution electrocatalysts for large-scale applications.

Keywords: Noble metal-free, Electrocatalysts, Alkaline, Oxygen evolution reaction

1. INTRODUCTION

Hydrogen is widely regarded as a promising alternative fuel due to its zero carbon emissions and high gravimetric energy density (140 MJ kg^{-1}) [1]. Although the global hydrogen production market was valued at approximately USD 120 billion in 2020, current production methods still rely heavily on steam methane reforming and coal gasification, which involve significant greenhouse gas emissions. In this context, electrochemical water splitting powered by renewable energy sources, such as solar and wind, has emerged as a sustainable and promising production method [2]. Industrial water electrolysis operating below 100°C can be divided into three categories: proton exchange membranes water electrolysis (PEMWE), anion exchange membrane water electrolysis (AEMWE), and alkaline water electrolysis (AWE). Currently, only AWE and PEMWE have been successfully commercialized. However, conventional AWE employs thick, porous diaphragms that necessitate precise pressure balancing to prevent gas crossover (H_2 and O_2). Furthermore, it suffers from low operating current densities (< 0.5 A cm^{-2}) due to high ohmic resistance, which limits the operational flexibility and

✉ **Gyeongbae Park; gpark@kitech.re.kr**

Gyeongbae Park and Da-Un Han contributed equally to this work.

results in lower hydrogen purity. The produced gas also contains alkaline mist, requiring additional purification equipment. While PEMWE adopts thin, dense proton exchange membranes, enabling high current density operation, high-purity gas production, and superior dynamic responsiveness. Its acidic environment mandates the use of expensive titanium bipolar plates and noble metal-based electrocatalysts. AEMWE effectively complements these technologies by integrating the structural advantages of PEMWE with the material flexibility of AWE. By utilizing a thin, dense anion exchange membrane, AEMWE enables a compact architecture that significantly reduces the ohmic losses and provides superior gas barrier properties, making it highly compatible with dynamic load fluctuations. Most importantly, the alkaline environment ensures compatibility with a wide range of non-noble metal catalysts and inexpensive metallic bipolar plates, positioning it as a highly promising and cost-effective technology for hydrogen production [3, 4].

However, several technical bottlenecks remain for the industrial-scale commercialization of AEMWE, including catalyst activity and durability, the chemical stability of membranes and ionomers, carbonate formation, and high interfacial resistance at elevated current densities. Electrocatalysts are essential to accelerate the kinetics of hydrogen and oxygen evolution reactions. However long-term durability must be ensured to reduce maintenance costs and the overall price of hydrogen. The anion exchange membrane (AEM) facilitates the transport of hydroxyl anions (OH-) while acting as a physical barrier to electrons and product gases. Developing membranes that simultaneously possess high mechanical stability and high ionic conductivity remains a challenge. For instance, incorporating excessive ion-exchange functional groups may enhance conductivity but often leads to a loss of mechanical integrity due to excessive water uptake and swelling. Similarly, ionomers, which bind the catalysts to the membrane and extend the reaction sites, face a trade-off: an excess ion-exchange groups improves conductivity but can cause dissolution or detachment at elevated temperatures. Furthermore, the dissolution of CO_2 from the air into the alkaline electrolyte forms bicarbonate (HCO_3^-) or carbonate (CO_3^{2-}) ions. These species have lower mobility than OH^-, thereby increasing ohmic resistance and deteriorating cell performance. Finally, operating at high current densities exacerbates interfacial and contact resistance, primarily due to gas bubble accumulation on the catalyst surface. This necessitates optimized water transport designs and gas pressure management. In this review, we focus on the activity and durability of diverse, noble metal-free, and cost-effective transition metal (TM)-based electrocatalysts designed to address these challenges [4–6].

Electrochemical water splitting involves the two-electron transfer hydrogen evolution reaction (HER) and the four-electron transfer oxygen evolution reaction (OER). The OER is inherently kinetically sluggish due to its complex multi-step proton-coupled electron transfer process, and is thus considered the primary bottleneck of the overall water splitting efficiency [7]. In alkaline media, the relevant electrochemical half-cell reactions and the net reaction, along with their standard equilibrium potential (25℃, 1 atm) as follows:

Cathode (HER): $4H_2O+4e^- \rightarrow 2H_2+4OH^-$ ($E° = -0.828$ V vs. SHE)

Anode (OER): $4OH^- \rightarrow O_2+2H_2O+4e^-$ ($E° = 0.401$ V vs. SHE)

Net reaction: $2H_2O \rightarrow 2H_2+O_2$ ($E°_{cell} = -1.229$ V)

The overpotential (η), which represents the additional energy required beyond the thermodynamic limit to overcome kinetic barriers such as activation energy and mass transport resistance, is defined as:

$$\eta = E_{applied} - E_{eq}$$

where $E_{applied}$ is the actual potential applied to the electrode and E_{eq} is the thermodynamic equilibrium potential. Minimizing overpotential for both HER and OER, particularly the latter, is crucial for improving the overall energy efficiency of the AEMWE system.

Conventionally, noble metal oxides such as IrO_x (η= 320 mV@10 mA cm^{-2} in 1 M NaOH) [8] and RuO_x (η=358 mV@10 mA cm^{-2} in 0.5 M KOH) [9] have been utilized as noble metal-based reference catalysts for the OER due to their high intrinsic activity. However, in alkaline media, these noble metal oxides are not necessarily the absolute benchmarks because several TM-based catalysts, most notably NiFe (oxy)hydroxides (η=209 mV@100 mA cm^{-2} in 1 M KOH) [10] and Co_3O_4 (230 mV@10 mA cm^{-2} in 1 M KOH) [11], have demonstrated comparable or even superior performance and stability. Consequently, the research focus for alkaline

AEMWE has shifted toward cost-effective alternatives that do not rely on scarce noble metals. Recently, extensive research has focused on TM-based electrocatalysts, including oxides [12,13], hydroxides [14–18], sulfides [19,20], selenides [21,22], phosphides [23–25], nitrides [26,27], and carbides [28,29]. These materials are promising candidates for OER due to their tunable electronic structures, rich surface chemistry, and structural versatility. To overcome the inherent limitations of single-component catalysts, various strategies such as elemental substitution [30,31], interface engineering [28,32–34], defect engineering [15,33,35] have been investigated to facilitate charge transfer, increase the density of active sites, and optimize electronic configurations. The development of such high-performance catalysts is essential for making scalable and economical water splitting systems feasible. In this regard, this paper reviews the fundamental mechanisms of OER in alkaline media and summarizes recent progress in various TM-based electrocatalysts. Finally, current challenges and future perspectives for the field are discussed.

2. MECHANISMS OF OER IN ALKALINE MEDIUM

The OER process in alkaline electrolytes involves the transfer of four hydroxide anions and four electrons to generate a single oxygen molecule, a process intrinsically linked to the redox cycling of the catalytic active sites. To date, three primary OER mechanisms have been proposed: adsorbate evolution mechanism (AEM), lattice oxygen mechanism (LOM), and oxide path mechanism (OPM) [36].

2.1 Adsorbate Evolution Mechanism (AEM)

The AEM is the most conventionally accepted pathway for OER electrocatalysts in alkaline media (Fig. 1a). The reaction initiates on a hydroxyl-covered catalyst surface (M-OH). The deprotonation of the M-OH group by an OH^- ion in the solution forms an M=O intermediate:

$$M\text{-}OH+OH^- \rightarrow M=O+H_2O+e^-$$

This is followed by the formation of a M-OOH intermediate through reaction with another OH^- ion:

$$M=O+OH^- \rightarrow M\text{-}OOH+e^-$$

Subsequently, deprotonation leads to the formation of a M-OO species:

$$M\text{-}OOH+OH^- \rightarrow M\text{-}OO+H_2O+e^-$$

Finally, the O_2 (OO) is released and the active site is regenerated by the adsorption of an OH^- ion:

$$M\text{-}OO+OH^- \rightarrow M\text{-}OH+O_2+e^-$$

For an ideal catalyst, the difference in Gibbs free energy (ΔG) for each step would be exactly 1.23 eV, the theoretical thermodynamic potential for OER.

Unfortunately, in real catalysts, these energy differences are not uniform. Furthermore, independently optimizing the adsorption energy of a single intermediate is challenging because these energies are intrinsically linked by linear scaling relation, typically expressed as follows [37]:

$$\Delta G_{OOH} - \Delta G_{OH} = 3.2 \pm 0.2 \text{ eV}$$

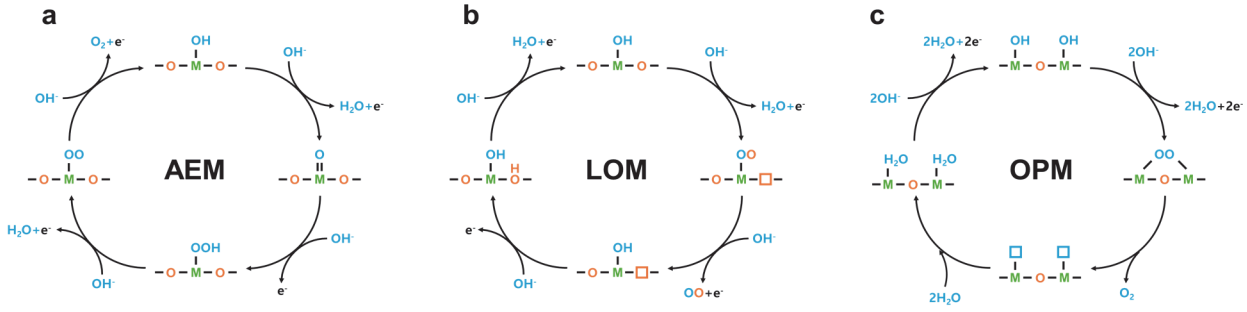

Fig. 1. Proposed mechanisms of oxygen evolution reaction in alkaline medium: (a) adsorbate evolution mechanism and (b) lattice oxygen mechanism, and (c) oxide path mechanism. Reproduced with permission from IOP Publishing Ltd (2020) Ref. [36].

2.2 Lattice Oxygen Mechanism (LOM)

The LOM involves the direct participation and coupling of lattice oxygen atoms (Fig. 1b). Initially, the active site is hydroxylated (M-OH). First step involves the deprotonation of OH group accompanied by the formation of an O-O bonding utilizing lattice oxygen:

$$O_{lattice}\text{-M-OH}+OH^- \rightarrow V_O\text{-M-OO}+H_2O+e^-$$

Upon the release of O_2 (OO), one of the resulting oxygen vacancies (V_O) is filled:

$$V_O\text{-M-OO}+OH^- \rightarrow V_O\text{-M-OH}+O_2+e^-$$

Subsequently, another vacancy site is occupied by OH^- ion from the electrolyte:

$$V_O\text{-M-OH}+OH^- \rightarrow \text{OH-M-OH}+e^-$$

Finally, the bridging site is deprotonated to regenerate the initial state:

$$\text{OH-M-OH}+OH^- \rightarrow O_{lattice}\text{-M-OH}+H_2O+e^-$$

The vacancy-filling steps are critical for regenerating the initial active surface and preventing structural degradation, which is essential for long-term stability. In contrast to AEM, the LOM can bypass the theoretical overpotential limits imposed by the scaling relation, as the reaction intermediates do not follow the conventional adsorption energy correlation. Consequently, LOM-based electrocatalysts often exhibit superior OER performance [38].

2.3 Oxide Path Mechanism (OPM)

Beyond the conventional AEM and LOM, the OPM has emerged to explain the exceptional performance and stability of certain OER catalysts that surpass traditional theoretical limits [39]. Unlike the AEM, the OPM requires at least two adjacent hydroxylated metal sites (OH-M+M-OH). The process begins with the deprotonation of two OH groups and the subsequent formation of an O-O bond through the coupling of two M=O species:

$$\text{OH-M+M-OH}+2OH^- \rightarrow \text{M-OO-M}+2H_2O+2e^-$$

The O_2 molecule is then released, leaving behind two vacant sites (V_O):

$$\text{M-OO-M} \rightarrow V_O\text{-M+M-}V_O+O_2$$

These vacant sites are subsequently filled by water molecules:

$$V_O\text{-M+M-}V_O+2H_2O \rightarrow H_2O\text{-M+M-OH}_2$$

Which are then deprotonated by OH- ions to restore the initial surface:

$$H_2O\text{-M+M-OH}_2+2OH^- \rightarrow \text{OH-M+M-OH}+2H_2O+2e$$

Notably, the OPM proceeds without the formation of an M-OOH intermediate formation or the direct participation of lattice oxygen, providing a unique pathway for high-performance OER electrocatalysts.

3. TRANSITION METAL (TM)–BASED ELECTROCATALYSTS FOR OER

Among the diverse classes of TM-based OER electrocatalysts, TM oxides have been the most extensively studied. This is primarily due to their well-established synthesis protocols, exceptional structural diversity-encompassing spinel, perovskite, rock salt, bixbyite, and amorphous phases-and robust long-term stability under harsh electrochemical conditions. [40]. TM hydroxides, particularly oxyhydroxides and layered double hydroxides (LDHs), have garnered significant attention owing to their highly tunable compositions. These materials offer versatility through the incorporation of various metal ions within the brucite-like layers and the exchange of intercalated anions between the layers [41]. In contrast, TM chalcogenides (sulfides, selenides) have emerged as efficient OER electrocatalysts due to their superior electrical conductivity compared to their oxides counterparts, along with their unique surface chemistry [42]. Similarly, TM phosphides exhibit promising OER performance, attributed to their distinct electronic structures and notable corrosion resistance [43]. Furthermore, TM nitrides have received growing interest because of their tailorable structural and electronic properties

[44]. Finally, TM carbides are considered as promising candidates for OER due to their synergistic combination of high electrical conductivity, exceptional high mechanical strength, and chemical stability [45].

3.1 TM Oxides

TM oxides exhibit remarkable durability in harsh OER environments, even in the presence of Cl^- anion. Malek et al. developed a Ni_xCr_yO catalyst composed of mixed Ni and Cr oxides, which demonstrates exceptional OER performance via dynamic surface reconstruction (Fig. 2a) [46]. Interestingly, the Ni_xCr_yO catalyst showed enhanced activity after a 1,000 h stability test at 10 mA cm^{-2}. Specifically, the initial overpotentials of 350 and 450 mV required to reach 100 and 500 mA cm^{-2} decreased to 270 and 320 mV, respectively (Fig. 2b). Furthermore, the catalyst exhibited superior long-term stability, exceeding 475 h at 100 mA cm^{-2} and 280 h at 500 mA cm^{-2} in 1 M KOH. X-ray photoelectron spectroscopy (XPS) analysis revealed the oxidation of Ni^{2+} into Ni^{3+} and Ni^{4+} (Fig. 2c), accompanied by near-complete disappearance of Cr 2p signal (Fig. 2d). This indicates the selective leaching of Cr from the catalyst surface, a process further supported by an increase in double-layer capacitance (C_{dl}) and electrochemically active surface area (ECSA), which rose from 0.18 to 1.06 mF and 4.5 to 26.5 cm^2, respectively. Even in seawater (Red Sea water with 1 M KOH), the Ni_xCr_yO catalyst maintained its performance, requiring overpotentials of 370 and 460 mV for 100 and 500 mA cm^{-2}, respectively, with a negligible overpotential increase (<20 mV) for 1,500 h at 10 mA cm^{-2} (Fig. 2e).

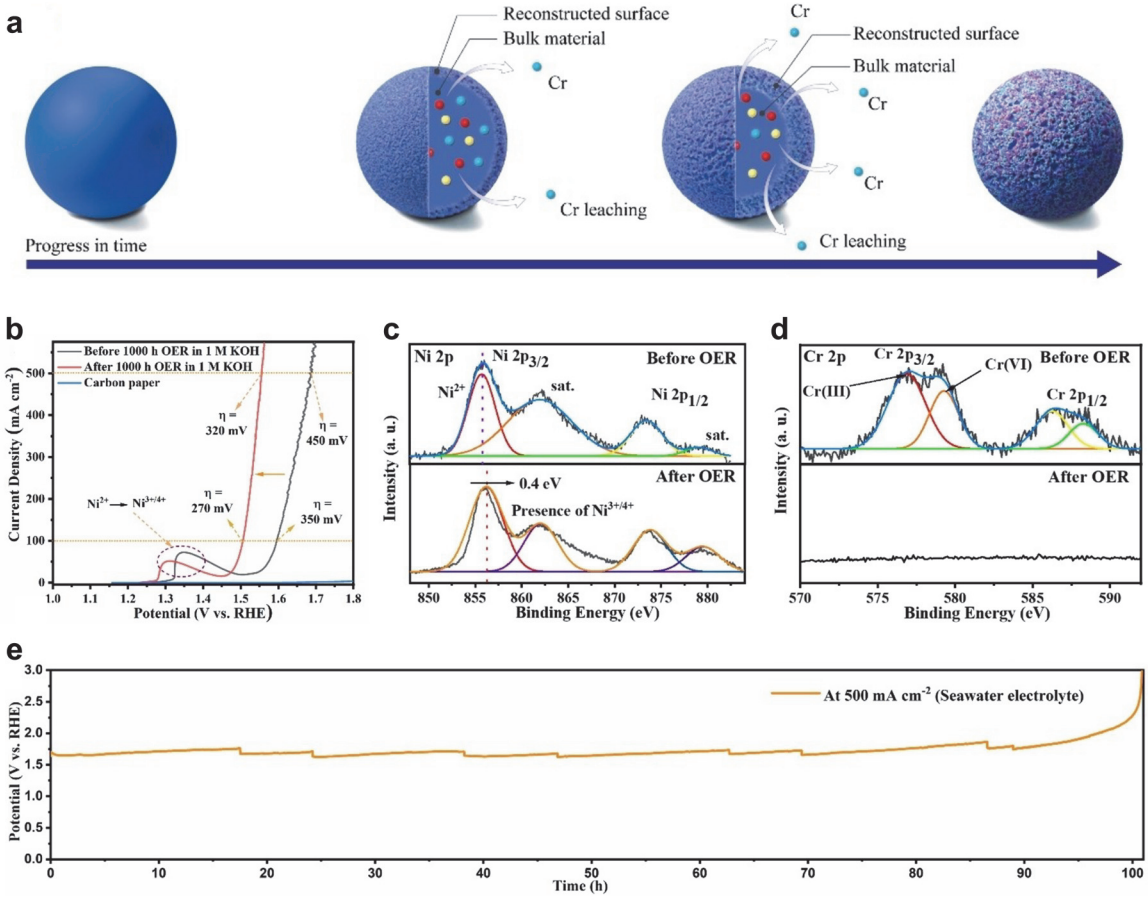

Fig. 2. Highly durable Ni_xCr_yO electrocatalyst. (a) Schematic diagram of surface reconstruction of Ni_xCr_yO electrocatalyst and (b) linear sweep voltammetry (LSV) curves of Ni_xCr_yO electrocatalyst before and after 1,000 h continuous OER in 1 M KOH. High resolution XPS spectra of (c) Ni 2p and (d) Cr 2p. (e) 100 h long-term stability test in seawater at 500 mA cm^{-2}. Reproduced with permission from Wiley-VCH GmbH (2023). Ref. [46].

Doping is another effective strategy to optimize the electronic structure of electrocatalysts, thereby facilitating higher activity. He et al. synthesized Ni,Fe co-doped MoO_2 nanospheres via a hydrothermal method [47]. In 1 M KOH at 10 mA cm^{-2}, the Ni,Fe co-doped MoO_2, exhibited a significantly lower overpotential (249 mV) compared to pristine MoO_2 (319 mV), Ni-doped MoO_2 (290 mV), and Fe-doped MoO_2 (279 mV). The corresponding Tafel slopes were 58.66, 64.99, 90.16, and 97.06 mV dec^{-1}, respectively, confirming that the Ni, Fe co-doped MoO_2 possesses the most favorable OER kinetics. XPS analysis showed that doping induces the oxidation of Mo ions, with the average valence state increasing in the order: Fe-doped MoO_2 (5.52) > Ni,Fe co-doped MoO_2 (5.49) > Ni-doped MoO_2 (5.38) > MoO_2 (4.92). Raman spectroscopy further revealed the development of hydroxyl groups and adsorbed water peaks after OER process, a phenomenon most prominent in the Ni,Fe co-doped MoO_2, indicating the OER occurs more effectively on the Ni,Fe co-doped MoO_2 surface. Chronopotentiometry tests demonstrated that Ni doping dramatically enhances long-term stability, which is further improved by Fe co-doping, showing almost no potential increase over 80 h. To explain these improvements, virtual energetic span (δE^V) was calculated to estimate the turnover frequency (TOF). The calculated δE^V for MoO_2, Fe-doped MoO_2, Ni-doped MoO_2 are 1.63. 0.44, and 0.99 eV, respectively, which indicates the activity is in sequence of Fe-doped MoO_2, Ni-doped MoO_2, and MoO_2. Additionally, free energies of intermediates were calculated, and it was revealed that the M-OH formation step is downhill for Ni-doped MoO_2 while Fe-doped MoO_2 and MoO_2 show uphill. Thus, synergetic effects of downhill M-OH formation energy in Ni-doping site and the highest TOF in Fe-doping site makes highly effective and durable Mo-based OER electrocatalysts.

Heterostructure formation can also surpass the intrinsic limitations of single-component catalysts through interfacial electron transfer and charge redistribution. Wang et al. synthesized $NiFe_2O_4$ nanoflakes on the tips of $NiCo_2O_4$ nanoneedles on Ni foam (NF) by successive hydro/ solvothermal reactions, followed by annealing [48]. This hierarchical structure derived from Ni(Co)x and NiFe-MIL53 MOF precursors exhibited a low overpotential of 265 mV at 50 mA cm^{-2} and exceptional stability for 100 h at 1 A cm^{-2}. The outstanding performance is attributed to three factors: (i) the heterojunction between $NiCo_2O_4$ and $NiFe_2O_4$ increases the density of state (DOS) at the Fermi level, enhancing conductivity and intermediate adsorption, (ii) interfacial electron transfer from Fe to Co and Ni facilitates surface reconstruction into active (oxy)hydroxide species (e.g., CoOOH and FeOOH), and (iii) the hierarchical architecture enhances hydrophilicity and provides abundant edge active sites.

3.2 TM Hydroxides

Among various hydroxides, layered double hydroxides (LDHs) have attracted significant attention due to their facile synthesis, compositional diversity, and excellent OER performance. LDHs can accommodate multiple metal ions within their structure, which often leads to synergistic effects that enhance catalytic activity. Yadav et al. prepared sea urchin-like NiCo LDH by a hydrothermal method using $NiCl_2{\cdot}6H_2O$, $CoCl_2{\cdot}6H_2O$, and urea [49]. Interestingly, increasing the reaction time from 4 to 12 h resulted in a decrease in crystallite size from 13.7 to 6.8 nm and a corresponding increase in specific surface area from 124.63 to 155.37 m^2 g^{-1}. Due to this increased surface area, the catalyst reacted for 12 h exhibited lower overpotentials of 300 and 360 mV for 25 and 100 mA cm^{-2}, respectively, outperforming the 4 h counterpart (350, 460 mV for 25, 100 mA cm^{-2}, respectively). Similarly, Bera et al. synthesized V-doped NiCo LDH through a simple coprecipitation method [50]. The V-doped NiCo LDH required a low overpotential of only 280 mV to reach 10 mA cm^{-2}, significantly lower than those of NiCo LDH (322 mV), $Ni(OH)_2$ (412 mV), and $Co(OH)_2$ (501 mV).

Beyond elemental substitution, introducing oxygen vacancy (V_O) is a potent strategy to boost electrocatalytic performance. Li et al. synthesized CoNiFe LDH containing V_O through the sacrificial co-precipitation of a CoNiFe-MOF followed by *in-situ* reconstruction under an electric field (Fig. 3a) [51]. Under an applied potential of 1.45 V (vs. RHE.) in 1 M KOH, Co, Ni, and Fe atoms were gradually etched and redeposited as hydroxides, which simultaneously transformed into oxyhydroxides. XPS analysis confirmed the formation of NiOOH (Fig. 3b) and CoOOH (Fig. 3c). All peaks in Fe 2p spectra are matched with Fe^{3+} oxidation state (Fig. 3d). Notably, the O 1s spectrum showed a larger peak area at 531.1 eV for the reconstructed catalyst, indicating a higher density of oxygen coordination defects (Fig. 3e). This V_O-rich CoNiFe LDH exhibited superior OER performance compared to commercial

RuO_2, with overpotentials of 207 and 241 mV for 10 and 50 mA cm^{-2}, respectively (Fig. 3f, h). Low Tafel slope of 52.1 mV dec^{-1} (Fig. 3g, h), and negligible degradation at 10 mA cm^{-2} after 60 h in 1 M KOH were observed (Fig. 3i). Chemical treatment can also be employed to induce V_O. Liu et al. used a $NaBH_4$ reduction process to generate abundant V_O in NiFe LDH [52]. Electron paramagnetic resonance spectroscopy and high-resolution transmission electron microscopy (HRTEM) confirmed the presence of these vacancies. XPS analysis revealed a positive shift (0.4 eV) in the Ni 2p binding energy and a negative shift (0.3 eV) in the Fe 2p peak, suggesting a modulation of electronic structure where electron density is redistributed from Ni to Fe. NiFe LDH with V_O achieved a remarkably low overpotential of 195 mV at 10 mA cm^{-2}, and Tafel slope of 47.9 mV dec^{-1}. DFT calculations identified the Fe site as the primary active site and demonstrated that V_O accelerates that rate-determining step (RDS), transformation of M-OH to M-O, by lowering the energy barrier from 2.55 to 2.08 eV.

Finally, the theoretical limitations of the AEM can be circumvented through heterostructure engineering. Gao et al. demonstrated that the scaling relation (ΔG_{OOH}-ΔG_{OH}= 3.2±0.2 eV) can be lowered to 2.75 eV by forming NiO/NiFe LDH heterostructure [53]. This catalyst, prepared via pulsed laser ablation of NiFe alloy in urea solution, followed by electrochemical oxidation (Fig. 4a-c), exhibited an extremely low overpotential of 205 mV at a current density of 30 mA cm^{-2} (Fig. 4d), Tafel slope of 30 mV dec^{-1} (Fig. 4e), and stability for 10 h at a current density of 20 mA cm^{-2} (Fig. 4f). Spin-polarized DFT+U calculations revealed that intermediates can adsorb simultaneously on both the NiFe LDH and NiO surfaces (Fig. 4g, h). This dual-site adsorption breaks the conventional scaling relation, reducing the theoretical overpotential to 0.2 V, whereas pristine NiFe LDH remains limited by a higher theoretical overpotential (0.36 V) due to its adherence to 3.2 eV scaling relation (Fig. 4i).

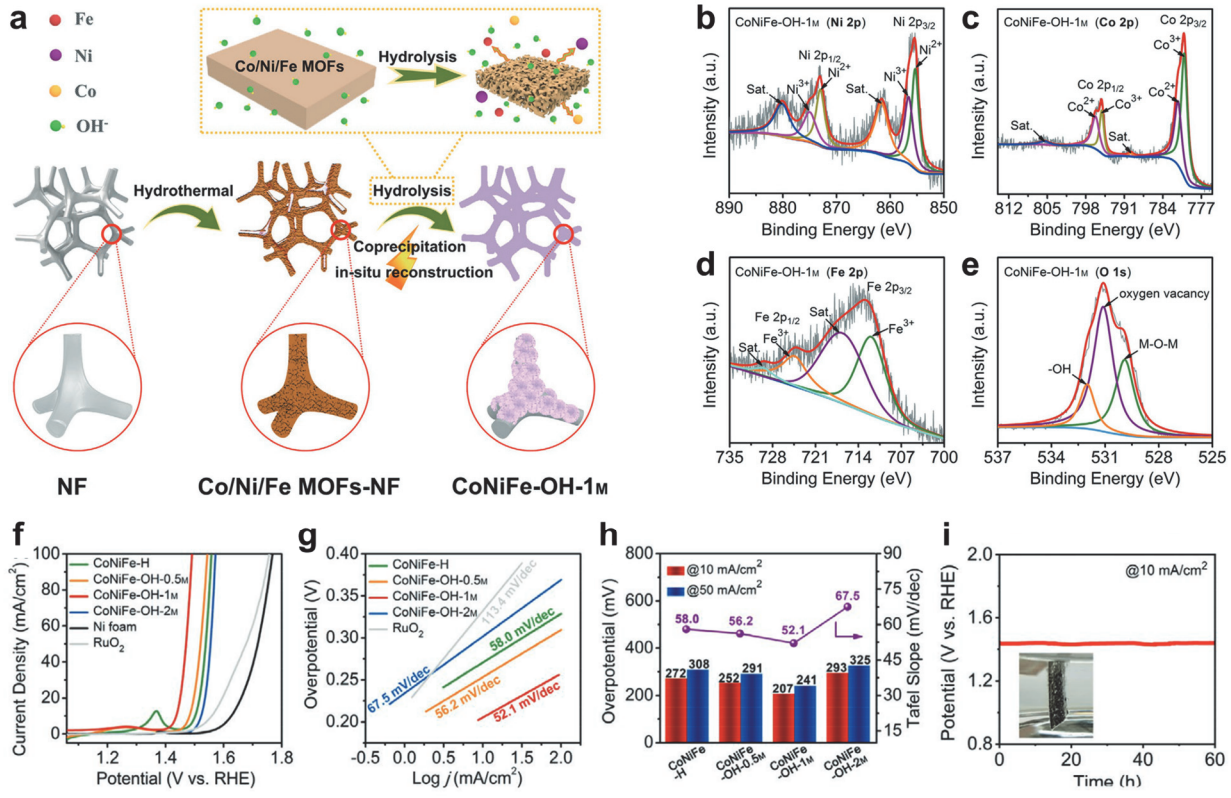

Fig. 3. Oxygen vacancy formation in ternary CoNiFe LDH in KOH under external voltage. (a) Schematic diagram of oxygen vacancy formation in ternary CoNiFe LDH. High resolution XPS spectra for (b) Ni 2p, (c) Co 2p, (d) Fe 2p, and (e) O 1s. OER electrocatalytic properties. (f) LSV curves, (g) Tafel slopes, (h) comparison charts of overpotential at 10 and 50 mA cm^{-2} and Tafel slopes, (i) chronopotentiometry curve for CoNiFe LDHs and RuO_2. Reproduced with permission from Wiley-VCH GmbH (2021). Ref. [51].

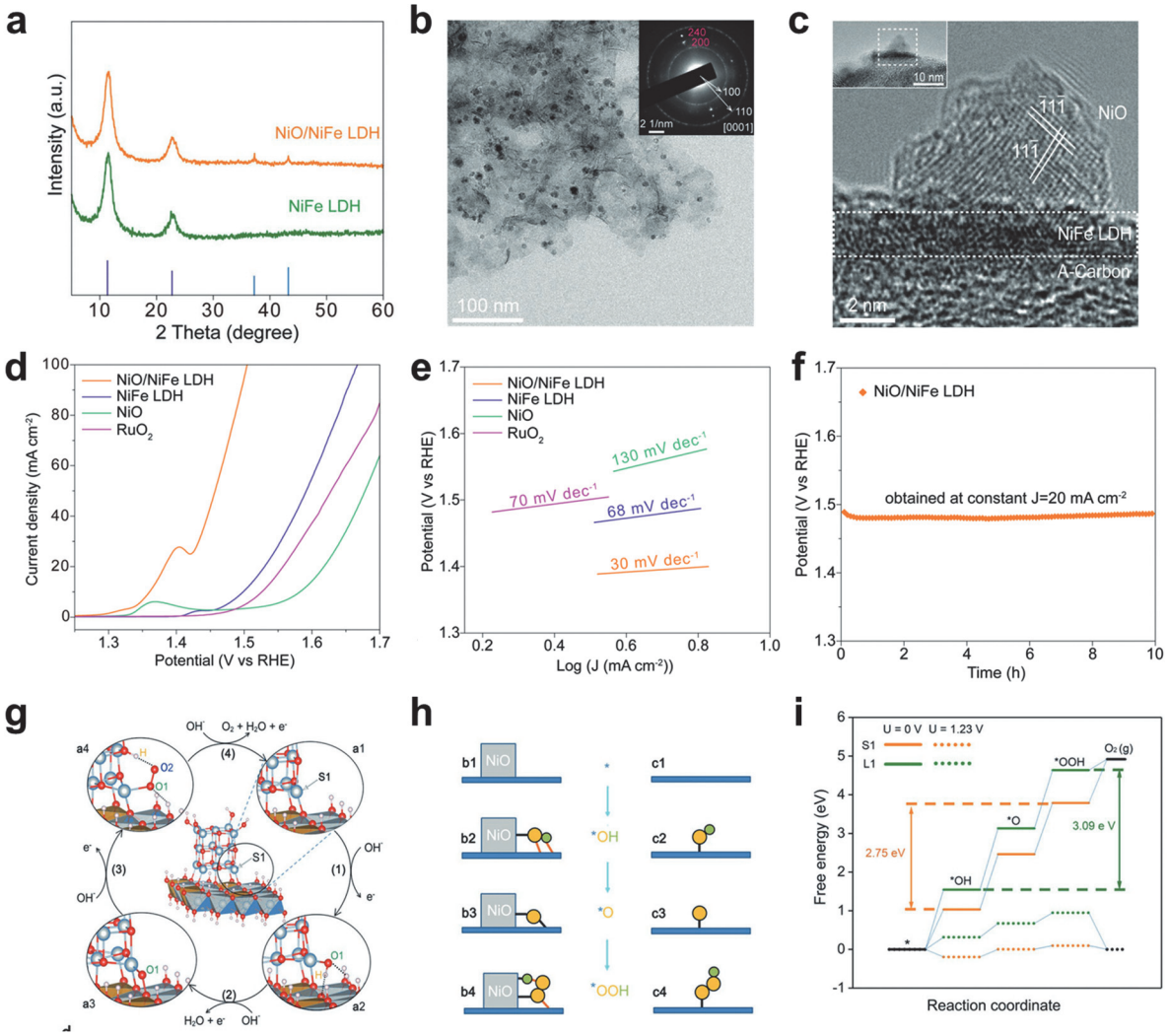

Fig. 4. NiO/NiFe LDH heterostructured electrocatalysts. (a) XRD pattern, (b) TEM image, and (c) HRTEM image showing interface between NiO and NiFe LDH. Electrochemical OER properties of NiO/NiFe LDH. (d) LSV curves, (e) Tafel slopes, and (f) long-term stability plots. (g) 3D and (h) 2D schematic diagram of the OER pathway through trimiensional adsorption of intermediates at NiO/NiFe LDH interface. (i) The Gibbs free energy diagram of the OER process with and without NiO. Reproduced with permission from Wiley-VCH GmbH (2019). Ref. [53].

3.3 TM Chalcogenides

TM chalcogenides (S, Se, and Te) have drawn much attention as OER electrocatalysts due to their low cost and high electrical conductivity. Heteroatom doping is a widely adopted strategy to modulate their catalytic performance. Mao et al. synthesized (Fe,Co)-doped Ni_3S_4 nanosheets on NF by two-step hydrothermal process, followed by sulfurization with Na_2S [54]. The dual-doped Ni_3S_4 exhibited lower overpotentials of 230 and 280 mV for 10 and 100 mA cm^{-2}, respectively, outperforming Fe-doped Ni_3S_4 (257 and 307 mV), Co-doped Ni_3S_4 (260 and 317 mV), and Ni_3S_4 (268 and 357 mV). The Tafel slope for the (Fe,Co)-doped Ni_3S_4 was 63.2 mV dec^{-1}, which was markedly lower than that of its counterparts, indicating accelerated charge transfer kinetics. Long-term stability was confirmed by chronopotentiometry, showing only a 22 mV overpotential increase after 360 h at 20 mA cm^{-2}, and LSV curve difference between before and after cyclic voltammetry tests, showing little deviation. Similarly, Huang et al. synthesized Co-doped $(Ni,Fe)_{1+x}S$ by stepwise electrodeposition and immersion, followed by annealing [55]. This catalyst demonstrated superior OER activity with an overpotential of only 164

mV at 10 mA cm^{-2} and a low Tafel slope of 23.2 mV dec^{-1}, which is superior to Co-doped $Ni_{1+x}S$ (216 mV, 33.8 mV dec^{-1}), Co-doped $Fe_{1+x}S$ (219 mV, 28.3 mV dec^{-1}), $(Ni,Fe)_{1+x}S$ (251 mV, 39.8 mV dec^{-1}), and RuO_2 (276 mV, 48.0 mV dec^{-1}). XPS analysis revealed that Co incorporation shifted the binding energies of Ni and Fe toward higher values of 0.20 and 0.32 eV, respectively, indicating an increase in their valence states. Furthermore, the presence of polysulfides (S_n^{2-}), which are beneficial for OER, was confirmed and found to persist even after the OER process. Overall water splitting activity was evaluated with Co-doped $(Ni,Fe)_{1+x}S$ as the anode and $MoNi_4/MoO_2$ as the cathode. The cell needs 1.60 V to obtain a current density of 100 mA cm^{-2} and the cell works over 1,200 h at 200 mA cm^{-2}.

Electrocatalytic activity can also be improved by constructing heterostructure interfaces that induce strong electronic interactions. Wang et al. developed core-shell structured $Ni_xS_y@MnO_xH_y$ nanorods on NF [56]. Comprehensive analysis (XPS, X-ray absorption near edge structure spectra, Fourier transformed extended X-ray absorption fine structure spectra) revealed abundant Mn-S bonds at the interface, facilitating strong electronic coupling. The MnO_xH_y shell also served as a protective shell, inhibiting the corrosion of the Ni_xS_y core. Consequently, the catalyst required overpotentials of only 326, 347, and 356 mV for current densities of 100, 300, and 500 mA cm^{-2}, respectively. In another study, Huang et al. synthesized Fe-doped NiS/NiS_2 heterostructured microspheres by etching Prussian blue analogues (PBA) [57]. The NiS/NiS_2 interfaces facilitated charge rearrangement, optimizing the Gibbs free energy of the reaction intermediates. XPS analysis showed a positive shift in the Ni 2p binding energy (0.25 eV) and a higher Ni^{3+}/Ni^{2+} ratio value (1.64) compared to Fe-doped NiS_2 (1.39), which is advantageous for the OER process (Fig. 5a). Strong Fe-S bonding (Fig. 5b) and the presence of both S^{2-} and S_2^{2-} species (Fig. 5c) further demonstrated strong interfacial electronic interactions. The Fe-doped $NiS-NiS_2$ catalyst achieved an overpotential of 270 mV for a current density of 50 mA cm^{-2} (Fig. 5d) with low Tafel slope of 84.21 mV dec^{-1} (Fig. 5e), and a small charge transfer resistance (3.38 Ω). The LSV curves before and after 1,000 continuous CV cycles showed almost perfect overlap and negligible degradation was observed in the chronoamperometry plots at 50 mA cm^{-2} for 12 h, indicating the excellent OER stability of the catalyst (Fig. 5f). DFT calculations identified the RDS as the formation of M-OOH from M-O (Fig. 5g), with the Fe-doped $NiS-NiS_2$ showing the lowest energy barrier (1.79 eV) among all compared samples (Fig. 5h-j).

In addition to TM sulfides, TM selenides have been extensively explored. Esmailzadeh et al. investigated the effect of pulse frequency during the electrodeposition of NiSe on NF [58], finding that high-surface-area agglomerated sheets formed at optimum frequencies provide superior performance (306, 318, 330 mV for 100, 150, 200 mA cm^{-2}). Li et al. demonstrated that Fe doping in $NiSe_2$ not only increases the number of active sites but also introduces lattice defects, which alter the intrinsic activity [59]. The $Ni_{0.9}Fe_{0.1}Se_2$ catalyst required an overpotential of 285 mV for 10 mA cm^{-2} with Tafel slope of 90 mV dec^{-1}, and showed a doubled double-layer capacitance (C_{dl}) compared to pristine $NiSe_2$. Han et al. showed that excellent OER performance could be achieved through a facile selenization of commercial stainless steel (SUS304), which contains Fe, Co, Ni, and Cr [60]. SUS304 foil annealed at 400°C required an overpotential of 284.3 mV with Tafel slope of 42 mV dec^{-1}, and maintained stability for over 160 h at 10 mA cm^{-2}.

3.4 TM Phosphides

TM phosphides are essentially interstitial compound where the P atoms occupy the lattice interstices of the TM, increasing metal-metal spacing and resulting in unique electronic configurations. Liu et al. prepared Fe_2P nanoparticle-embedded Co_2P nanosheets (Fe_2P-Co_2P) on cobalt foam [61]. The synthesis involved air calcination of cobalt foam to obtain cobalt oxide, followed by the electrodeposition of FeOOH nanosheets and subsequent phosphorization with NaH_2PO_2 under an Ar atmosphere. XPS analysis revealed a positive shift of 0.2 eV in the Co 2p binding energy and a negative shift of 0.1 eV in the P 2p peaks for Fe_2P-Co_2P compared to pristine Co_2P. Consequently, the Fe_2P-Co_2P catalyst exhibited remarkably low overpotentials of 185, 243, 291, and 317 mV to achieve 10, 100, 500 and 1,000 mA cm^{-2}, respectively, along with a low Tafel slope of 51 mV dec^{-1}. Multistep chronopotentiometry confirmed the robust stability of the catalyst across a wide range of current densities. Similarly, Chen et al. evaluated the OER activity of heterostructured Fe-doped $Ni_2P-Ni_5P_4$ supported on N-doped carbon [62]. XPS spectra indicated that Fe doping induces electron transfer from Ni to P. Fe-doped Ni_2P-

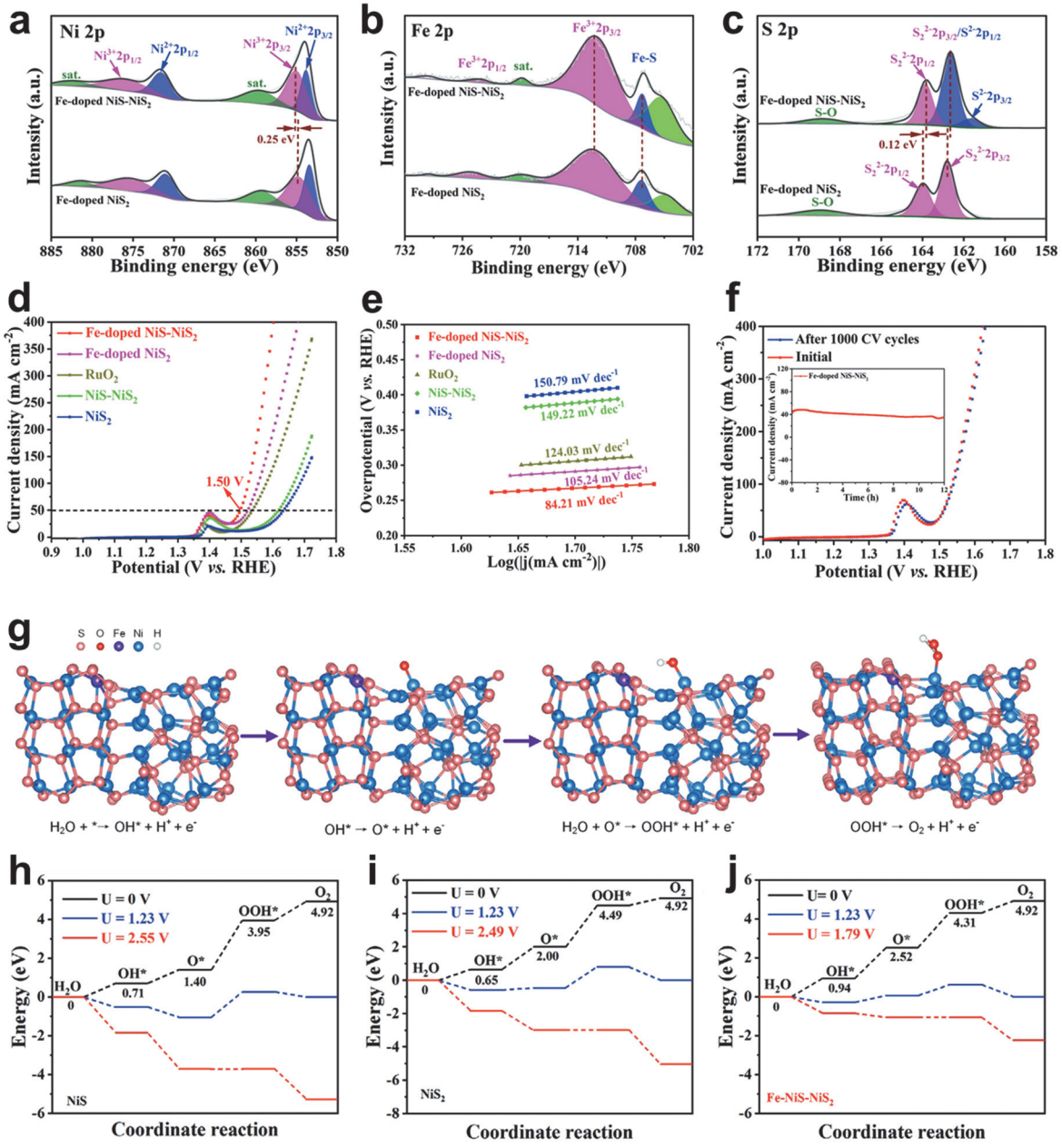

Fig. 5. Fe-doped NiS-NiS_2 OER electrocatalysts. High-resolution XPS spectra of Fe-doped NiS-NiS_2. (a) Ni 2p, (b) Fe 2p, and (c) S 2p. Electrochemical performance of Fe-doped NiS-NiS_2. (d) LSV curves, (e) Tafel slopes, and (f) LSV curves before and after 1,000 CV cycles, the inset shows chronoamperometry plot. (g) Schematic illustration of four step OER process on Fe-doped NiS-NiS_2. Gibbs free adsorption energy diagrams of (h) NiS_2, (i) NiS, and (j) Fe-doped NiS-NiS_2. Reproduced with permission from Wiley-VCH GmbH (2022). Ref. [57].

Ni_5P_4 shows lower overpotential of 280 mV for a current density of 50 mA cm^{-2} with Tafel slope of 60.8 mV dec^{-1}, while undoped Ni_2P-Ni_5P_4 shows 401 mV with Tafel slope of 96.6 mV dec^{-1}, indicating Fe doping can enhance intrinsic performance of OER of nickel phosphides. Theoretical investigations via DFT calculations revealed that the RDS for Fe-doped Ni_2P-Ni_5P_4 is the formation of M-OOH from M-O, with a significantly lower energy barrier (1.72 eV) at the Fe site compared to pristine Ni_2P-Ni_5P_4 (2.33 eV). Furthermore, band structure calculations showed that Fe doping shifts the d-band center toward the Fermi energy from -1.808 to -1.765 eV, which strengthens the binding affinity with reaction intermediates.

Recently, Tan et al. demonstrated that a heterojunction between CoP and Ni_5P_4 can significantly enhance the OER performance of NiFe LDH [63]. This hierarchical catalyst NiFe LDH@CoP-Ni_5P_4 was synthesized through a multi-step process involving hydrothermal growth of cobalt precursors, phosphorization, and final electrodeposition of NiFe LDH (Fig. 6a-e). XPS analysis confirmed electron transfer from NiFe LDH to CoP-Ni_5P_4, the resulting NiFe LDH@CoP-Ni_5P_4 catalyst showed exceptional activity, requiring overpotentials of 179, 221, and 246 mV for current densities of 10, 50, and 100 mA cm^{-2}, respectively (Fig. 6f). NiFe LDH@CoP-Ni_5P_4 electrocatalysts also exhibited ultralow Tafel slope of 38.4 mV dec^{-1} (Fig. 6g) and exceptional stability, where only 2 mV overpotential increase at 100 mA cm^{-2} after 3,000 cycles of LSV test, and minimal change of current density (200 mA cm^{-2}) during 100 h was observed (Fig. 6h). The Mott-Schottky measurements suggested the formation of an n-n heterojunction at CoP/Ni_5P_4 interface (Fig. 6i). Due to higher Fermi level of CoP relative to Ni_5P_4, band bending occurs, facilitating interfacial charge transport and carrier separation, which ultimately promotes OER on the surface. While Tan et al. deposited TM hydroxides onto TM phosphides, Chen et al.

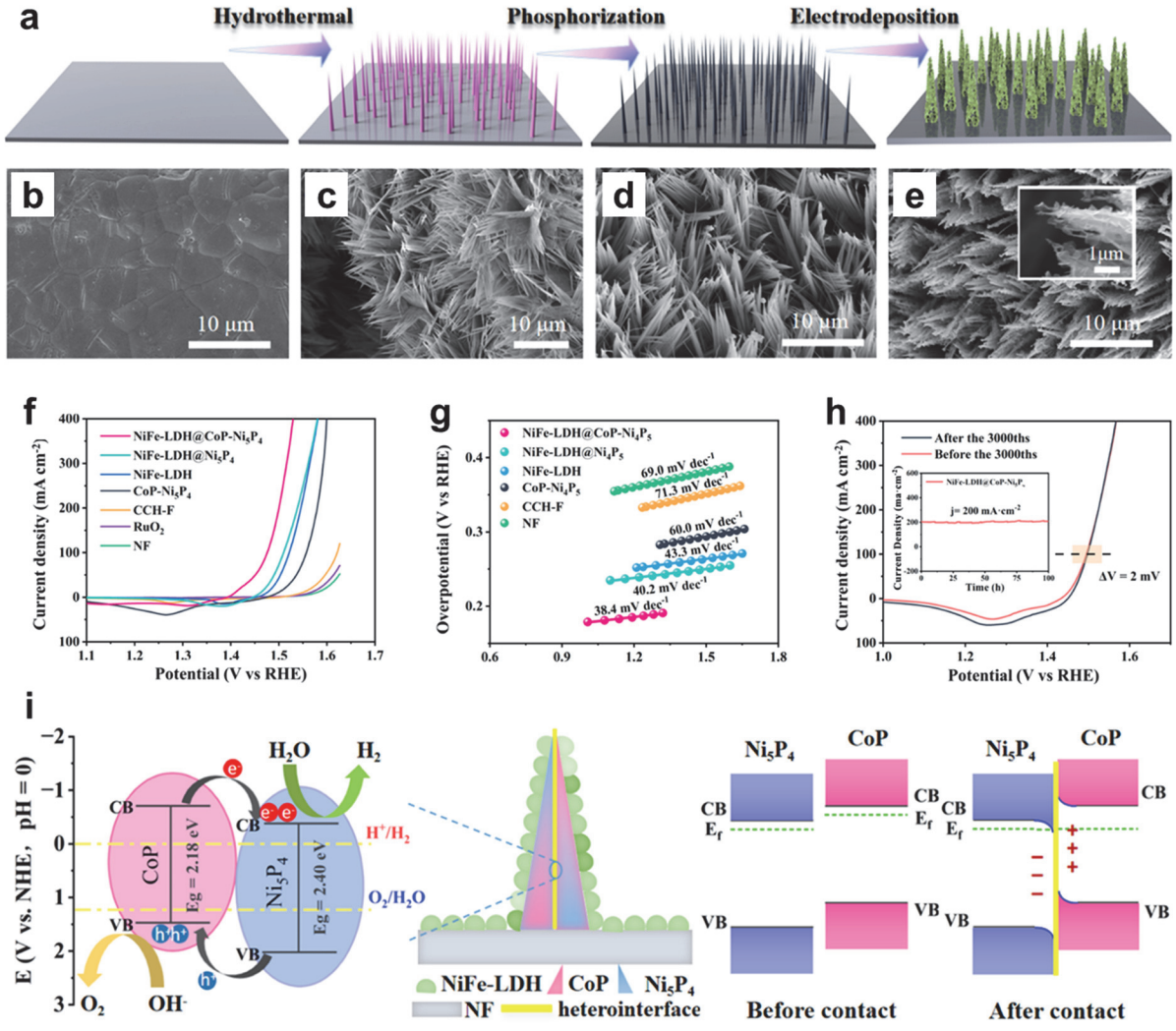

Fig. 6. NiFe LDH@CoP-Ni_5P_4 heterojunction nanoarrays electrocatalyst. (a) Schematic diagram of synthesis process and (b-e) corresponding SEM images. OER performances of electrocatatalysts. (f) LSV curves, (g) Tafel slopes, and (h) durability of NiFe LDH@CoP-Ni_5P_4. (i) Illustration of heterojunction between CoP and Ni_5P_4. Reproduced with permission from American Chemical Society (2024). Ref. [63].

explored the reverse sequence by forming NiP_x nanoparticles on the $Co(OH)_2$ nanosheets [64]. XRD and Raman spectroscopy indicated a unit cell shrinkage of $Co(OH)_2$ in the $Co(OH)_2/NiP_x$ composite, while XPS showed a negative shift (0.2-0.4 eV) in the Co 2p binding energy, signifying strong electronic interaction. This catalyst required overpotentials of 236, 304, and 340 mV for a current density of 10, 100, and 400 mA cm^{-2}, respectively. Tafel slope of $Co(OH)_2/NiP_x$ (52 mV dec^{-1}) was the smallest among the control samples (87 mV dec^{-1} for $Co(OH)_2$, 237 mV dec^{-1} for NiP_x). Beyond electronic modulation, the introduction of NiP_x significantly enhanced the surface hydrophilicity, as evidenced by a drastic reduction in the water contact angle from 137.5° to 18.9°. This improved wetting and facilitated the rapid release of oxygen bubbles, further boosting the OER process.

3.5 TM Nitrides

TM nitrides have emerged as highly promising electrocatalysts due to their high intrinsic electrical conductivity and excellent corrosion-resistance, which contribute to sustained long-term activity. Chen et al. synthesized metallic Co_4N nanowire arrays on carbon cloth by nitridation of Co(OH)F nanowire arrays by NH_3 [65]. While Co(OH)F nanowire and Co_3O_4 nanowires required overpotentials of 375 and 320 mV to reach a current density of 10 mA cm^{-2}, respectively, Co_4N nanowires array exhibited a low overpotential of 257 mV to obtain 10 mA cm^{-2} with a Tafel slope of 44 mV dec^{-1}. HRTEM revealed the formation of a thin (1-2 nm) surface oxide layer, suggesting that the sequential oxidation of surface Co to CoOOH and CoO_2 serves as the active OER mechanism. Similarly, Yu et al. prepared Fe_xN on graphene-coated NF by direct nitridation of $Fe(NO_3)_3$ precursor [66]. The resulting mesoporous catalyst required an overpotential of only 238 mV for a current density of 10 mA cm^{-2} with a Tafel slope of 44.5 mV dec^{-1}, and exceptional durability during 17 h chronoamperometry test.

The construction of heterostructures with LDHs is a particularly effective strategy for achieving industrial-scale OER performance. Zhai et al. developed NiMoN/NiFe LDH catalyst arrays with outstanding performance at high current densities [67]. NiMoN nanoarrays were prepared by the NH_3 nitridation of $NiMoO_4 \cdot H_2O$ on nickel foam grown by hydrothermal reaction. Then, amorphous NiFe LDH nanosheets were electrodeposited on as-prepared NiMoN nanorods (Fig. 7a). XPS analysis confirmed strong electronic interactions between the amorphous NiFe LDH nanosheets and the NiMoN nanorod arrays, evidenced by binding energy shift in Ni 2p (Fig. 7b), Mo 3d (Fig. 7c), and Fe 2p (Fig. 7d) spectra. Remarkably, the NiMoN/NiFe LDH electrocatalyst required only 236 and 266 mV to deliver industrial-level current densities of 500, and 1,000 mA cm^{-2}, respectively, which is lower than those of NiFe LDH (351 and 406 mV), NiMoN (492 and 575 mV), $NiMoO_4$ (465 and 548 mV), and Ni foam (719 mV) (Fig. 7e). Low Tafel slope of 42.2 mV dec^{-1} was also obtained, which is lower than counterparts: NiFe LDH (83.2 mV dec^{-1}) and NiMoN (170.9 mV dec^{-1}) (Fig. 7f). This catalyst also showed a high Faradaic efficiency (~ 98.5 %) and maintained stability for over 250 h at 1,000 mA cm^{-2} (Fig. 7g). In 1 M KOH at 25°C, the bifunctional catalyst required cell voltages of only 1.70 and 1.77 V to achieve 500, and 1,000 mA cm^{-2}, respectively (Fig. 7h). In industrial conditions where 30% KOH electrolyte is used at high temperature (80°C), the NiMoN/NiFe LDH showed better activities of 1.54 and 1.62 V for 500 and 1,000 mA cm^{-2} (Fig. 7i), with no evident fluctuation at a current density of 1,000 mA cm^{-2} over 50 h (Fig. 7j). In-situ Raman and UV-Vis spectroscopy identified γ-Ni(Fe)OOH as the active species, which formed more readily on the heterojunction interface. Furthermore, ^{18}O isotope labeling combined with differential electrochemical mass spectrometry confirmed that the reaction follows the LOM, bypassing the scaling relation limitations of the conventional AEM.

Additionally, ANM_3-type antiperovskite nitrides (where A and M are transition metals) have gained increasing attention. Cui et al. identified $CuNCo_{2.4}V_{0.6}$ as an optimal composition with an overpotential of 235 mV at 10 mA cm^{-2} [68]. Zhu et al. reported that $CuNCo_3$ nanosheets and $CoN_{0.73}Co_3$ nanowires on NF serve as excellent bifunctional electrodes for OER and HER, respectively [69]. A two-electrode water electrolysis cell using these catalysts achieved current densities of 10 and 100 mA cm^{-2} at 1.53 and 1.79 V. Post-stability analysis via XRD and HRTEM confirmed that the surface of these nitrides reconstructs into a CoOOH active phase, which is responsible for the high catalytic efficiency.

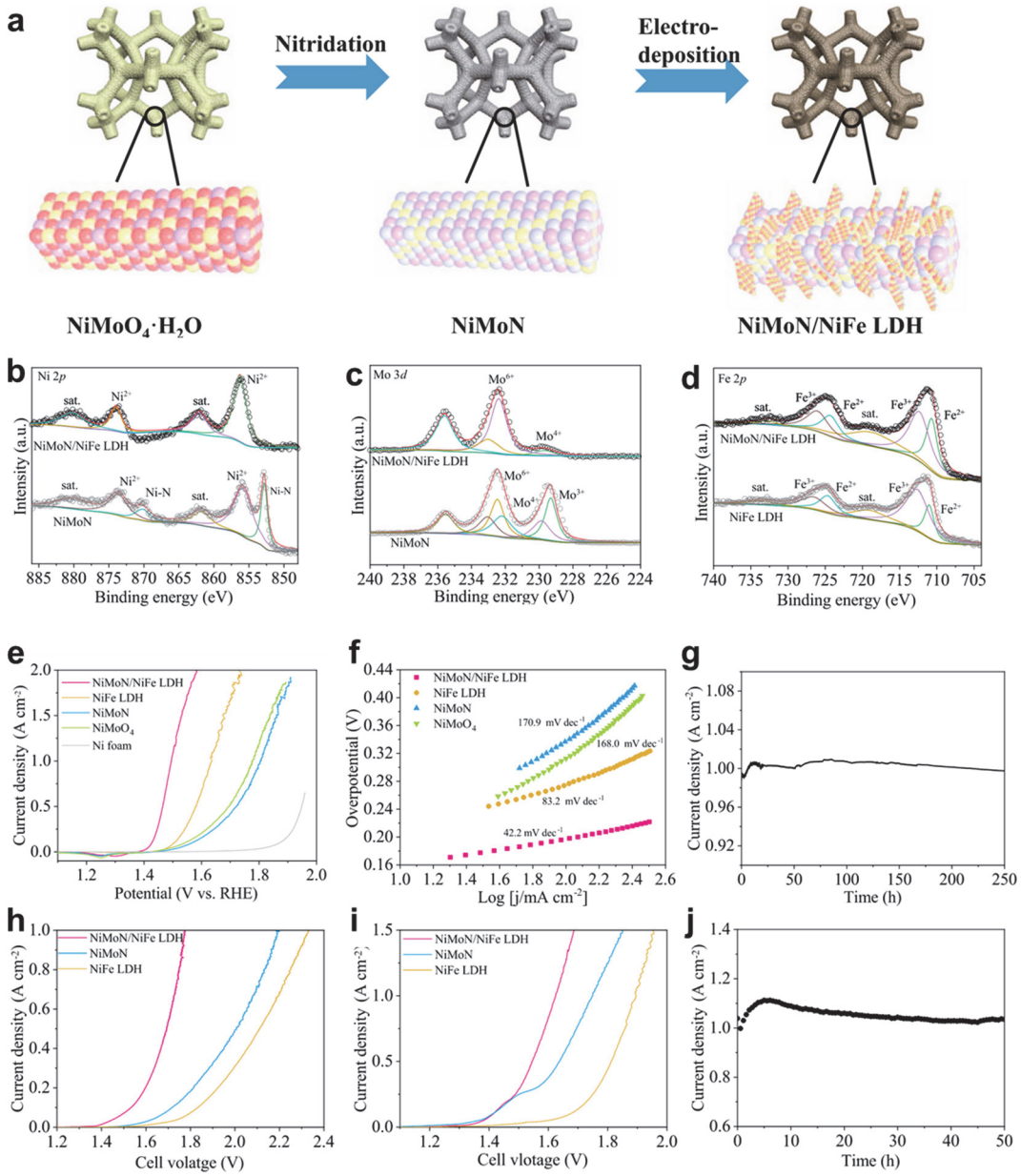

Fig. 7. NiMoN/NiFe LDH electrocatalyst for industrial scale water splitting. (a) Schematic illustration of synthesis route of NiMoN/NiFe LDH. (b) Ni 2p, (c) Mo 3d, and (d) Fe 2p high-resolution XPS spectra of NiMoN/NiFe LDH. (c) LSV curves, (f) Tafel slope, and (g) long-term stability at 1,000 mA cm^{-2}. Overall water splitting performance of NiMoN/NiFe LDH in (h) 1 M KOH at 25℃, and (i) 30% KOH at 80℃. (j) Chronoamperometry curve of overall water splitting in 30 % KOH at 80℃. Reproduced with permission from Proceedings of the Springer Nature (2023). Ref. [67].

3.6 TM Carbides

Among various metal carbides, molybdenum carbide (Mo_2C) has attracted interest because its electronic structure resembles that of platinum-group metals. Jayawardana et al. synthesized N-doped Co nanoparticle-decorated Mo_2C (N-Co/Mo_2C) by simple precipitation, followed by the pyrolysis of a mixture containing ammonium molybdate, TMA, melamine, and cobalt chloride [70]. N-Co/Mo_2C electrocatalyst showed low overpotential of 198 mV at 10 mA cm^{-2} with Tafel slope of 64 mV $dec^{-1,}$ exhibiting negligible activity decay over 100 h chronoamperometry test at 10 mA cm^{-2}. Recently, Sial

et al. developed NiCoFe carbide on NF using direct laser writing, which significantly reduced the production time to mere minutes [71]. Unlike conventional structures, these laser-induced carbides possessed distorted crystal lattices with a high density of defect sites. The resulting defective NiCoFe carbide exhibited an overpotential of 198 mV at current density of 10 mA cm^{-2} with Tafel slope of 106 mV dec^{-1}, which is much lower than the overpotentials of monometallic carbides synthesized by the same procedure. DFT calculations revealed that the presence of lattice defects lowered the theoretical overpotential from 1.69 V (pristine) to 0.97 V (defective), thereby enhancing the intrinsic OER activity.

Co_2P/Mo_2C heterojunctions have also emerged as efficient bifunctional electrocatalysts. Sun et al. synthesized Co_2P/Mo_2C@N-doped carbon heterostructure using SiO_2 nanospheres as templates, which were subsequently removed by acid etching (Fig. 8a) [72]. The electrocatalyst required overpotentials of 209, 270, and 350 mV to reach current densities of 10, 50, and 100 mA cm^{-2}, respectively. The Tafel slope (91 mV dec^{-1}) was considerably lower than those of RuO_2 (132 mV dec^{-1}), Mo_2C@N-doped carbon (140 mV dec^{-1}), and Co_2P@N-doped carbon (169 mV dec^{-1}) (Fig. 8b), and the catalyst maintained its overpotential for 30 h continuous chronopotentiometry test (Fig. 8c). Furthermore, the catalyst

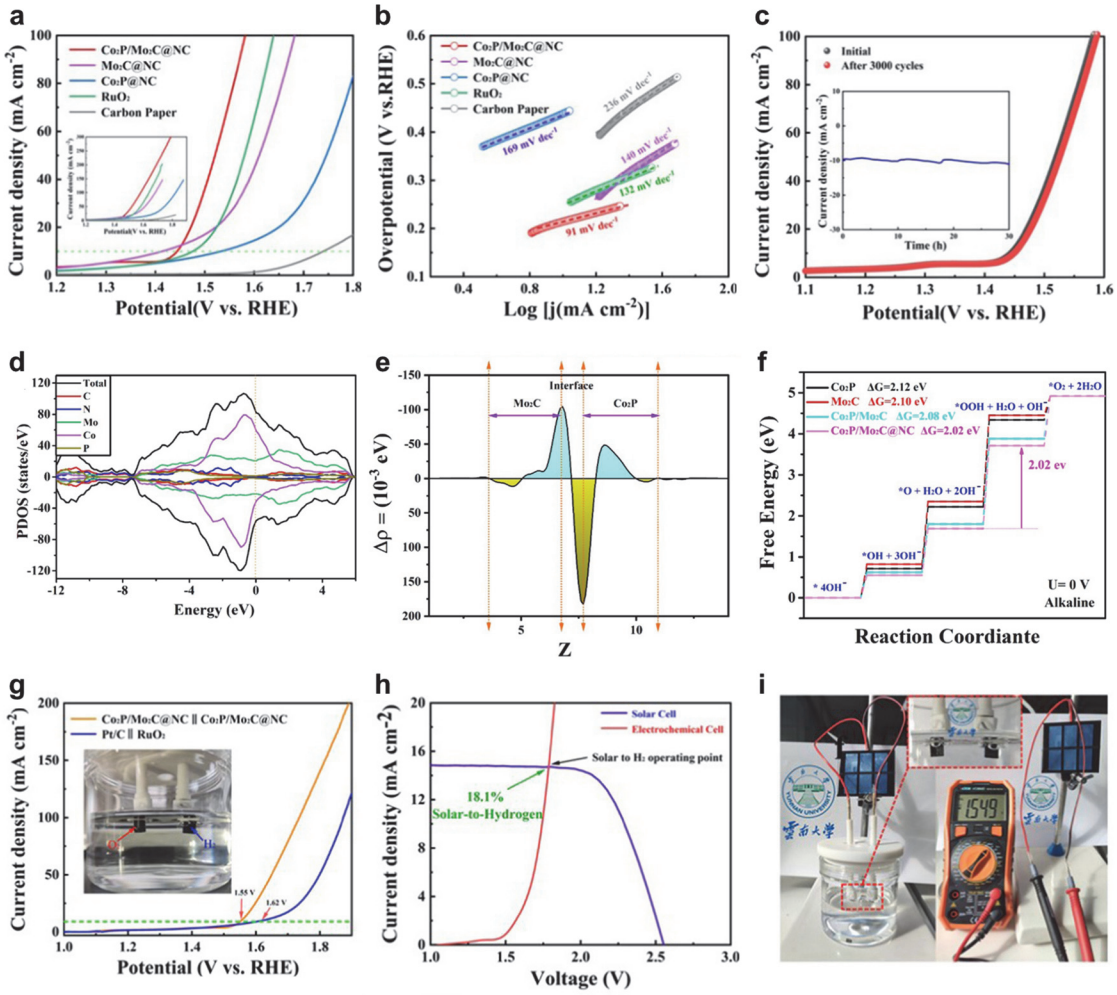

Fig. 8. Co_2P/Mo_2C@N-doped carbon electrocatalyst. (a) LSV curves, (b) Tafel slope (c) polarization curves before and after 3,000 continuous cycles (inset: chronoamperometry curve at 10 mA cm^{-2}) of Co_2P/Mo_2C@N-doped carbon. Projected density of states, (e) plane-averaged electrostatic potential drop across the Co_2P/Mo_2C@N-doped carbon interface. (f) Gibbs free adsorption energies of OER intermediates. (g) Polarization curves for two-electrode cell. (h) J-V curves for solar cell and electrochemical cell. (i) Digital camera image of water electrolyzer directly connected to solar cell. Reproduced with permission from Proceedings of Elsevier (2022). Ref. [72].

demonstrated excellent bifunctionality, requiring only 1.55 V to achieve a current density of 10 mA cm^{-2} in a two-electrode overall water splitting cell near 100% Faradaic efficiency. The projected DOS analysis indicated that the Co orbitals in Co_2P/Mo_2C heterostructure exhibit a higher DOS near the Fermi level compared to pristine Co_2P, suggesting that the heterojunction facilitates enhanced electron transfer (Fig. 8d). Charge density difference calculations further confirmed an electron mitigation from Mo to Co at the interface (Fig. 8e). Gibbs free energy diagrams identified the formation of M-OOH from M-O as the RDS, with the heterostructure reducing the energy barrier (2.02 eV) compared to Co_2P (2.12 eV) (Fig. 8f). Remarkably, when integrated with GaAs solar cell under AM 1.5 G irradiation, this system achieved a solar-to-hydrogen conversion efficiency of 18.1 %, demonstrating its potential for practical, light-driven hydrogen production (Fig. 8g-i).

4. SUMMARY AND OUTLOOK

Electrochemical water splitting represents one of the most promising technologies for carbon-free hydrogen production. Among the various electrolysis systems, AEMWE has garnered significant attention due to its compatibility with cost-effective electrocatalysts and its operational flexibility under power fluctuations. However, the sluggish kinetics of the OER remains a critical bottleneck, necessitating the urgent development of highly efficient and durable catalysts. This review has summarized the primary OER mechanisms: AEM, LOM, and OPM. While the AEM is conventionally used to describe the stepwise adsorption/desorption of oxygenated intermediates, it is inherently limited by the scaling relation between M-OOH and M-OH species. In contrast, the LOM bypasses these constraints by involving lattice oxygen, thereby eliminating the mandatory M-OOH formation step. Furthermore, the OPM has been proposed to explain the exceptional activity and stability of next-generation catalysts, as it avoids both lattice oxygen depletion and the scaling -limited intermediates. This review further discussed various TM-based electrocatalysts, including oxides, hydroxides, chalcogenides, phosphides, nitrides, and carbides. To enhance catalytic performance, diverse strategies such as multimetal doping, interface engineering, and defect modulation have been employed. These approaches effectively enhance electrical conductivity, maximize the electrochemically active surface area, and optimize the adsorption energies of reaction intermediates via electronic structure regulation. Despite extensive progress, several challenges must be addressed to advance the field toward practical application.

· Mechanistic understanding: Although AEM, LOM, and OPM provide theoretical frameworks, a complete mechanistic understanding remains elusive. Future research should prioritize in-situ and operando characterization—including XPS, Raman spectroscopy, and X-ray absorption spectroscopy (XAS)—to monitor the dynamic evolution of active sites and intermediates under real-time reaction conditions.

· Degradation and mitigation strategies: To achieve practical durability, future research must align enhancement strategies with specific failure modes of TM-based catalysts. Metal leaching and dissolution can be mitigated by multimetal doping to stabilize the crystal lattice. Mechanical detachment and the resulting growth in interfacial resistance caused by gas evolution can be addressed through interface engineering to enhance catalyst-substrate adhesion. Additionally, loss of conductivity and excessive surface reconstruction can be managed via defect regulation, ensuring the maintenance of robust active sites and efficient charge transfer paths even under harsh oxidative conditions.

· Industrial-scale evaluation: Most catalysts are currently evaluated in three-electrode configurations at low current densities (10 mA cm^{-2}) and ambient temperatures. However, industrial AEMWE operates at high temperatures (> 60°C) and high current densities (> 1 A cm^{-2}) for thousands of hours. Future studies must evaluate catalyst performance within membrane-electrode assemblies under these rigorous conditions to ensure practical viability.

· Large-area fabrication and catalyst integration: Scalable manufacturing must be directly linked to the catalyst/electrode concepts. While catalyst-ink deposition is applicable to large areas, it often suffers from binder-induced resistance and catalyst detachment. To address this, the direct growth or surface-corrosion methods discussed for TM-based catalysts/electrodes should be optimized to ensure high compositional tunability. Future efforts should focus on integrating scalable defect engineering (e.g., plasma treatment or chemical etching) during the electrode fabrication process to ensure that the high intrinsic activity of the catalyst is preserved at the industrial scale.

ORCID

Gyeongbae Park https://orcid.org/0000-0002-4812-1405

ACKNOWLEDGEMENT

This work was supported by the Technology Innovation Program (20019175) funded by the Ministry of Trade, Industry and Resources (MOTIR, Korea).

REFERENCES

[1] J. S. Kim, B. Kim, H. Kim, and K. Kang, *Adv. Energy Mater.*, **8**, 1702774 (2018). doi: https://doi.org/10.1002/aenm.201702774

[2] Z. Cai, X. Bu, P. Wang, J. C. Ho, J. Yang, and X. Wang, *J. Mater. Chem. A*, **7**, 5069 (2019). doi: https://doi.org/10.1039/c8ta11273h

[3] Z. Wei, M. Guo, and Q. Zhang, *Appl. Catal. B*, **322**, 122101 (2023). doi: https://doi.org/10.1016/j.apcatb.2022.122101

[4] Q. Xu, L. Zhang, J. Zhang, J. Wang, Y. Hu, H. Jiang, and C. Li, *EnergyChem*, **4**, 100087 (2022). doi: https://doi.org/10.1016/j.enchem.2022.100087

[5] I. Vincent and D. Bessarabov, *Renew. Sustain. Energy Rev.*, **81**, 1690 (2018). doi: https://doi.org/10.1016/j.rser.2017.05.258

[6] D. Li, A. R. Motz, C. Bae, C. Fujimoto, G. Yang, F. Y. Zhang, K. E. Ayers, and Y. S. Kim, *Energy Environ. Sci.*, **14**, 3393 (2021). doi: https://doi.org/10.1039/d0ee04086j

[7] J. Song, C. Wei, Z. F. Huang, C. Liu, L. Zeng, X. Wang, and Z. J. Xu, *Chem. Soc. Rev.*, **49**, 2196 (2020). doi: https://doi.org/10.1039/c9cs00607a

[8] C.C.L. McCrory, S. Jung, J. C. Peters, and T. F. Jaramillo, *J. Am. Chem. Soc.*, **135**, 16977 (2013). doi: https://doi.org/10.1021/ja407115p

[9] C. W. Tung, Y. Y. Hsu, Y. P. Shen, Y. Zheng, T. S. Chan, H. S. Sheu, Y. C. Cheng, and H. M. Chen, *Nat. Commun.*, **6**, 8106 (2015). doi: https://doi.org/10.1038/ncomms9106

[10] W. Zhao, H. Xu, H. Luan, N. Chen, P. Gong, K. Yao, Y. Shen, and Y. Shao, *Adv. Energy Mater.*, **12**, 2102372 (2022). doi: https://doi.org/10.1002/aenm.202102372

[11] R. Li, D. Zhou, J. Luo, W. Xu, J. Li, S. Li, P. Cheng, and D. Yuan, *J. Power Sources*, **341**, 250 (2017). doi: https://doi.org/10.1016/j.jpowsour.2016.10.096

[12] T. Kou, S. Wang, R. Shi, T. Zhang, S. Chiovoloni, J. Q. Lu, W. Chen, M. A. Worsley, B. C. Wood, S. E. Baker, E. B. Duoss, R. Wu, C. Zhu, and Y. Li, *Adv. Energy Mater.*, **10**, 2002955 (2020). doi: https://doi.org/10.1002/aenm.202002955

[13] X. Yu, C. Hu, P. Ji, Y. Ren, H. Zhao, G. Liu, R. Xu, X. Zhu, Z. Li, Y. Ma, and L. Ma, *Appl. Catal. B*, **310**, 121301 (2022). doi: https://doi.org/10.1016/j.apcatb.2022.121301

[14] Z. He, J. Zhang, Z. Gong, H. Lei, D. Zhou, N. Zhang, W. Mai, S. Zhao, and Y. Chen, *Nat. Commun.*, **13**, 2191 (2022). doi: https://doi.org/10.1038/s41467-022-29875-4

[15] Y. Hu, J. Zhou, L. Li, Z. Hu, T. Yuan, C. Jing, R. Liu, S. Xi, H. Jiang, J. Q. Wang, and L. Zhang, *J. Mater. Chem. A*, **10**, 602 (2022). doi: https://doi.org/10.1039/d1ta08938b

[16] Z. Yin, R. He, Y. Zhang, L. Feng, X. Wu, T. Wågberg, and G. Hu, *J. Energy Chem.*, **69**, 585 (2022). doi: https://doi.org/10.1016/j.jechem.2022.01.020

[17] S. Tao, Q. Wen, W. Jaegermann, and B. Kaiser, *ACS Catal.*, **12**, 1508 (2022). doi: https://doi.org/10.1021/acscatal.1c04589

[18] Y. Zhuo, D. Liu, L. Qiao, S. Chen, J. Lu, W. F. Ip, H. Pan, and Z. Wang, *Adv. Energy Mater.*, **13**, 2301921 (2023). doi: https://doi.org/10.1002/aenm.202301921

[19] C. Chen, Z. Zhou, J. Liu, B. Zhu, H. Hu, Y. Yang, G. Chen, M. Gao, and J. Zhang, *Appl. Catal. B*, **307**, 121209 (2022). doi: https://doi.org/10.1016/j.apcatb.2022.121209

[20] C. Tang, D. He, N. Zhang, X. Song, S. Jia, Z. Ke, J. Liu, J. Wang, C. Jiang, Z. Wang, X. Huang, and X. Xiao, *Energy Environ. Mater.*, **5**, 899 (2022). doi: https://doi.org/10.1002/eem2.12205

[21] S. Ibraheem, G. Yasin, A. Kumar, M. A. Mushtaq, S. Ibrahim, R. Iqbal, M. Tabish, S. Ali, and A. Saad, *Appl. Catal. B*, **304**, 120987 (2022). doi: https://doi.org/10.1016/j.apcatb.2021.120987

[22] R. Balaji, T. T. Nguyen, K. Harish, N. H. Kim, and J. H. Lee, *J. Mater. Chem. A*, **10**, 3782 (2022). doi: https://doi.org/10.1039/d1ta09932a

[23] M. I. Díez-García, G. Montaña-Mora, M. Botifoll, A. Cabot, J. Arbiol, M. Qamar, and J. R. Morante, *ACS Appl. Energy Mater.*, **6**, 5690 (2023). doi: https://doi.org/10.1021/acsaem.3c00032

[24] L. Wu, L. Yu, B. McElhenny, X. Xing, D. Luo, F. Zhang, J. Bao, S. Chen, and Z. Ren, *Appl. Catal. B*, **294**, 120256 (2021). doi: https://doi.org/10.1016/j.apcatb.2021.120256

[25] R. Liu, X. R. Shi, Y. Wen, X. Shao, C. Su, J. Hu, and S. Xu, *J. Energy Chem.*, **74**, 149 (2022). doi: https://doi.org/10.1016/j.jechem.2022.07.015

[26] J. Song, D. Yu, X. Wu, D. Xie, Y. Sun, P. Vishniakov, F. Hu, L. Li, C. Li, M. Yu. Maximov, K. M. El-Khatib, and S. Peng, *Chem. Eng. J.*, **437**, 135281 (2022). doi: https://doi.org/10.1016/j.cej.2022.135281

[27] D. Li, Y. Xing, R. Yang, T. Wen, D. Jiang, W. Shi, and S. Yuan,

ACS Appl. Mater. Interfaces, **12**, 29253 (2020).
doi: https://doi.org/10.1021/acsami.0c05219

[28] S. Yuan, M. Xia, Z. Liu, K. Wang, L. Xiang, G. Huang, J. Zhang, and N. Li, *Chem. Eng. J.*, **430**, 132697 (2022).
doi: https://doi.org/10.1016/j.cej.2021.132697

[29] Y. Xu, J. Yang, T. Liao, R. Ge, Y. Liu, J. Zhang, Y. Li, M. Zhu, S. Li, and W. Li, *Chem. Eng. J.*, **431**, 134126 (2022).
doi: https://doi.org/10.1016/j.cej.2021.134126

[30] H. N. Dhandapani, D. Mahendiran, A. Karmakar, P. Devi, S. Nagappan, R. Madhu, K. Bera, P. Murugan, B. R. Babu, and S. Kundu, *J. Mater. Chem. A*, **10**, 17488 (2022).
doi: https://doi.org/10.1039/d2ta04647d

[31] Y. Lin, H. Wang, C. Peng, L. Bu, C. Chiang, K. Tian, Y. Zhao, J. Zhao, Y. Lin, J. Lee, and L. Gao, *Small*, **16**, 2002426 (2020).
doi: https://doi.org/10.1002/smll.202002426

[32] X. Wang, X. Yu, J. Bai, G. Yuan, P. He, Y. Zhu, S. Wu, F. Qin, and L. Ren, *Electrochim. Acta*, **458**, 142524 (2023).
doi: https://doi.org/10.1016/j.electacta.2023.142524

[33] H. G. Gim, E. Park, J. Ha, J. Lee, Y. T. Kim, and J. Choi, *Mater. Today Energy*, **41**, 101526 (2024).
doi: https://doi.org/10.1016/j.mtener.2024.101526

[34] H. Chen, J. Li, L. Chen, G. Li, W. Zhao, K. Tao, and L. Han, *Inorg. Chem.*, **62**, 20194 (2023).
doi: https://doi.org/10.1021/acs.inorgchem.3c03115

[35] L. Wang, Y. Pan, D. Wu, X. Liu, L. Cao, W. Zhang, H. Chen, T. Liu, D. Liu, T. Chen, T. Ding, Y. Wang, C. Ding, C. Kang, C. Li, J. He, and T. Yao, *J. Mater. Chem. A*, **10**, 20011 (2022).
doi: https://doi.org/10.1039/d2ta02989h

[36] D. Antipin and M. Risch, *J. Phys. Energy*, **2**, 032003 (2020).
doi: https://doi.org/10.1088/2515-7655/ab812f

[37] I. C. Man, H. Su, F. Calle-Vallejo, H. A. Hansen, J. I. Martínez, N. G. Inoglu, J. Kitchin, T. F. Jaramillo, J. K. Nørskov, and J. Rossmeisl, *ChemCatChem*, **3**, 1159 (2011).
doi: https://doi.org/10.1002/cctc.201000397

[38] K. A. Jannath and H. A. Saputra, *Next Mater.*, **9**, 101164 (2025).
doi: https://doi.org/10.1016/j.nxmate.2025.101164

[39] R. Murugesan, N.C.S. Selvam, and A. Maruthapillai, *Catal. Sci. Technol.*, **15**, 6928 (2025).
doi: https://doi.org/10.1039/d5cy00724k

[40] L. Zhang, Q. Fan, K. Li, S. Zhang, and X. Ma, *Sustainable Energy Fuels*, **4**, 5417 (2020).
doi: https://doi.org/10.1039/d0se01087a

[41] C. Han, Y. Zhao, Y. Yuan, Z. Guo, G. Chen, J. Yang, Q. Bao, L. Guo, and C. Chen, *Int. J. Hydrogen Energy*, **63**, 918 (2024).
doi: https://doi.org/10.1016/j.ijhydene.2024.03.150

[42] M. Wang, L. Zhang, Y. He, and H. Zhu, *J. Mater. Chem. A*, **9**, 5320 (2021).
doi: https://doi.org/10.1039/d0ta12152e

[43] C. J. Huang, H. M. Xu, T. Y. Shuai, Q. N. Zhan, Z. J. Zhang, and G. R. Li, *Appl. Catal. B*, **325**, 122313 (2023).
doi: https://doi.org/10.1016/j.apcatb.2022.122313

[44] N. Ayasha, A. Ahuja, and S. Mitra, *ChemistrySelect*, **8**, e202300885 (2023).
doi: https://doi.org/10.1002/slct.202300885

[45] H. Wang, S. Zhu, J. Deng, W. Zhang, Y. Feng, and J. Ma, *Chin. Chem. Lett.*, **32**, 291 (2021).
doi: https://doi.org/10.1016/j.cclet.2020.02.018

[46] A. Malek, Y. Xue, and X. Lu, *Angew. Chem. Int. Ed.*, **135**, e202309854 (2023).
doi: https://doi.org/10.1002/ange.202309854

[47] H. He, H. Chen, J. Chen, C. Jia, J. Chen, J. Liang, X. Yao, L. Qin, Y. Huang, D. Chen, and Z. Wen, *Chem. Eng. J.*, **443**, 136339 (2022).
doi: https://doi.org/10.1016/j.cej.2022.136339

[48] X. Wang, J. Luo, Y. Tuo, Y. Gu, W. Liu, S. Wang, Y. Zhou, and J. Zhang, *Chem. Eng. J.*, **457**, 141169 (2023).
doi: https://doi.org/10.1016/j.cej.2022.141169

[49] P. S. Yadav, N. S. Yadav, S. D. Jituri, K. B. Pisal, P. B. Patil, S. S. Mali, J. V. Patil, C. K. Hong, H. Im, A. I. Inamdar, and S. H. Mujawar, *J. Phys. Chem. Solids*, **206**, 112860 (2025).
doi: https://doi.org/10.1016/j.jpcs.2025.112860

[50] K. Bera, A. Karmakar, S. Kumaravel, S. Sam Sankar, R. Madhu, H. N. Dhandapani, S. Nagappan, and S. Kundu, *Inorg. Chem.*, **61**, 4502 (2022).
doi: https://doi.org/10.1021/acs.inorgchem.2c00093

[51] X. Li, M. Hou, X. Qu, Y. Zhang, and M. Li, *Small*, **18**, 2104863 (2022).
doi: https://doi.org/10.1002/smll.202104863

[52] S. Liu, H. Zhang, E. Hu, T. Zhu, C. Zhou, Y. Huang, M. Ling, X. Gao, and Z. Lin, *J. Mater. Chem. A*, **9**, 23697 (2021).
doi: https://doi.org/10.1039/d1ta06263h

[53] Z. Gao, J. Liu, X. Chen, X. Zheng, J. Mao, H. Liu, T. Ma, L. Li, W. Wang, and X. Du, *Adv. Mater.*, **31**, 1804769 (2019).
doi: https://doi.org/10.1002/adma.201804769

[54] X. Mao, Y. Liu, Z. Chen, Y. Fan, and P. Shen, *Chem. Eng. J.*, **427**, 130742 (2022).
doi: https://doi.org/10.1016/j.cej.2021.130742

[55] Y. Huang, L. W. Jiang, H. Liu, and J. J. Wang, *Chem. Eng. J.*, **441**, 136121 (2022).
doi: https://doi.org/10.1016/j.cej.2022.136121

[56] P. Wang, Y. Luo, G. Zhang, Z. Chen, H. Ranganathan, S. Sun, and Z. Shi, *Nano-Micro Lett.*, **14**, 120 (2022).
doi: https://doi.org/10.1007/s40820-022-00860-2

[57] S. Huang, Q. Zhang, P. Xin, J. Zhang, Q. Chen, J. Fu, Z. Jin, Q. Wang, and Z. Hu, *Small*, **18**, 2106841 (2022).
doi: https://doi.org/10.1002/smll.202106841

[58] S. Esmailzadeh, T. Shahrabi, Gh. Barati Darband, and Y. Yaghoubinezhad, *Electrochim. Acta*, **334**, 135549 (2020).
doi: https://doi.org/10.1016/j.electacta.2019.135549

[59] Y. Li, R. Chen, D. Yan, and S. Wang, *Chem. Asian J.*, **15**, 3845 (2020).
doi: https://doi.org/10.1002/asia.202000860

[60] M. H. Han, Y. J. Ko, S. Y. Lee, C. Lim, W. H. Lee, M. W. Pin, J. H. Koh, J. Kim, W. Kim, B. K. Min, and H. S. Oh, *J. Power Sources*, **521**, 230953 (2022).
doi: https://doi.org/10.1016/j.jpowsour.2021.230953

[61] X. Liu, Y. Yao, H. Zhang, L. Pan, C. Shi, X. Zhang, Z. F. Huang, and J. J. Zou, *ACS Sustainable Chem. Eng.*, **8**, 17828 (2020).
doi: https://doi.org/10.1021/acssuschemeng.0c06987

[62] Q. Chen, Y. Yu, S. Zhou, L. Sha, G. Zhuang, P. Wang, and X. Han, *Inorg. Chem.*, **62**, 6518 (2023).
doi: https://doi.org/10.1021/acs.inorgchem.3c00703

[63] W. Tan, M. Qin, G. Ma, Z. Fan, X. Li, and X. Xin, *ACS Sustainable Chem. Eng.*, **12**, 5139 (2024).
doi: https://doi.org/10.1021/acssuschemeng.3c07722

[64] M. Chen, H. Li, C. Wu, Y. Liang, J. Qi, J. Li, E. Shangguan, W. Zhang, and R. Cao, *Adv. Funct. Mater.*, **32**, 2206407 (2022).
doi: https://doi.org/10.1002/adfm.202206407

[65] P. Chen, K. Xu, Z. Fang, Y. Tong, J. Wu, X. Lu, X. Peng, H. Ding, C. Wu, and Y. Xie, *Angew. Chem. Int. Ed.*, **54**, 14710 (2015).
doi: https://doi.org/10.1002/anie.201506480

[66] F. Yu, H. Zhou, Z. Zhu, J. Sun, R. He, J. Bao, S. Chen, and Z. Ren, *ACS Catal.*, **7**, 2052 (2017).
doi: https://doi.org/10.1021/acscatal.6b03132

[67] P. Zhai, C. Wang, Y. Zhao, Y. Zhang, J. Gao, L. Sun, and J. Hou, *Nat. Commun.*, **14**, 1873 (2023).
doi: https://doi.org/10.1038/s41467-023-37091-x

[68] J. Zhang, X. Zhao, L. Du, Y. Li, L. Zhang, S. Liao, J. B. Goodenough, and Z. Cui, *Nano Lett.*, **19**, 7457 (2019).
doi: https://doi.org/10.1021/acs.nanolett.9b03168

[69] L. Zhu, C. Li, H. Li, H. Li, Z. Wu, Y. Huang, X. Zhu, and Y. Sun, *J. Mater. Chem. A*, **10**, 15520 (2022).
doi: https://doi.org/10.1039/d2ta03313e

[70] H.M.C.M. Jayawardana, S. Meng, B. A. Yusuf, J. Jing, H. Ren, Q. Nie, J. Xie, M. Chen, and Y. Xu, *Mater. Today Chem.*, **43**, 102476 (2025).
doi: https://doi.org/10.1016/j.mtchem.2024.102476

[71] M.A.Z.G. Sial, M. Furquan, R. Hassan, Z. M. Bhat, U. Alam, Z. H. Yamani, and M. Qamar, *ACS Appl. Energy Mater.*, **8**, 9166 (2025).
doi: https://doi.org/10.1021/acsaem.5c00808

[72] P. Sun, Y. Zhou, H. Li, H. Zhang, L. Feng, Q. Cao, S. Liu, T. Wågberg, and G. Hu, *Appl. Catal. B*, **310**, 121354 (2022).
doi: https://doi.org/10.1016/j.apcatb.2022.121354